ELSEVIER

Journal of Nuclear Materials 304 (2002) 107–116

journal of nuclear materials

www.elsevier.com/locate/jnucmat

# Depletion of Fe and Cr within precipitates during Zircaloy-4 oxidation

Jong Hyuk Baek *, Yong Hwan Jeong

*Advanced Fuel Cladding Development, Korea Atomic Energy Research Institute, P.O. Box 105, Yuseong, Daejeon 305-600, South Korea*

Received 9 August 2001; accepted 21 May 2002

**Abstract**

Analyses of the oxide layers which were formed in a static autoclave of 400 °C steam after the heat-treatment to coarsen the precipitates were performed with the optical microscope, scanning electrical microscope (SEM), transmission electron microscope, electron probe micro-analyzer (EPMA), synchrotron X-ray diffractometer (XRD), and secondary ion mass spectroscope (SIMS), paying attention to the oxidation of Fe and Cr within $Zr(Fe,Cr)_2$ precipitates in Zircaloy-4. The oxide analyses were concentrated on the oxidized samples in the regime of pre- and post-transition. It could be confirmed from the SEM observation of the interfacial oxide that the Zr matrix was oxidized earlier than the precipitates. During the oxidation process, the unoxidized precipitates were incorporated in the interfacial oxide, and then the precipitates were oxidized gradually in the oxide layer. From EPMA, synchrotron XRD and SIMS analyses, the alloying elements such as Fe and Cr within precipitates exhibited differences in oxidation rate. It was found that the Fe depletion from precipitates in the initial stage stabilized the tetragonal $ZrO_2$ phase of the surrounding oxide and when the oxidation time increased, the depletion of Fe and Cr initiated the phase transformation of the oxide crystal structure from tetragonal $ZrO_2$ to monoclinic $ZrO_2$. All Fe within precipitates were depleted in the preference to Cr. It is thought that the overall corrosion rate of Zircaloy-4 can be governed mostly by the oxidation of $Zr(Fe,Cr)_2$ precipitates, and the oxidation rate of Fe was much faster than that of Cr in precipitates.


*PACS:* 42.81.B; 81.65.M; 81.65.K

## 1. Introduction

Zircaloy-4 alloy has been used as a fuel cladding material in pressurized water reactors since the 1960s. The primary metallurgical factors that have been found to correlate with the corrosion characteristics of Zircaloy-4 are the size and distribution of precipitates such as $Zr(Fe,Cr)_2$ [1–6]. The solubility of Fe and Cr in α-Zr is less than the common impurity levels. So, most of the Fe and Cr are always present in the form of precipitates.

Many researchers have suggested that the precipitates in the Zr matrix be incorporated into the oxide and oxidized gradually in it [7–14]. Pecheur et al. [7,8] indicated that the transformation of $ZrO_2$ in the oxide structure and the decrease of the Fe to Cr ratio in precipitates occurred during the process of oxidation. According to the hypotheses of Anada et al. [12,13] and Baek et al. [14], some of the Fe and Cr in the precipitates diffuses into the surrounding $ZrO_2$ and is then oxidized to Fe oxide and Cr oxide. The difference of the pilling-Bedworth ratio [15] between the Zr and alloying elements reduces the compressive stress heterogeneously in the surrounding $ZrO_2$ and the protectiveness to the inward diffusion of the oxygen ions. In their studies, they posited that the precipitates of an unoxidized state

* Corresponding author. Tel.: +82-42 868 8823; fax.: +82-42 682 0432/686 8346.

*E-mail address:* jhbaek@kaeri.re.kr (J.H. Baek).

0022-3115/02/$ - see front matter 
PII: S0022-3115(02)00903-0

existed in the oxide layer and then the Fe, Cr and Zr in the precipitates could be gradually oxidized to the Fe oxide, Cr oxide and Zr oxide, respectively. However, the details of this phenomenon were not completely agreed upon. The oxidation rate of alloying elements such as Fe and Cr within the precipitates has not verified since the phase relationships between these metal oxides and zirconium oxide are complicatedly dependent on the space coordinates of oxide film.

The objectives of this study are to clarify the oxidation rate of Fe and Cr in the precipitates and to explain the role of the precipitates in the oxidation process of Zr-based alloys. The Zircaloy-4 samples having coarsened precipitates were oxidized in 400 °C steam and the coarsened precipitates were characterized for the oxide specimens in the pre- and post-transition regimes using the optical microscopes, scanning electrical microscope (SEM), transmission electron microscope (TEM), electron probe micro-analyzer (EPMA), synchrotron X-ray diffractometer (XRD) and secondary ion mass spectroscope (SIMS).

## 2. Experimental procedures

### 2.1. Preparation of specimens

The materials investigated in this study were low-Sn Zircaloy-4 sheets, which were manufactured by Cezus and satisfied with ASTM B 352-92 GR60804. The chemical composition of this alloy is shown in Table 1. The oxidation of precipitates could be observed more easily in the coarsening state than in the as-received state. In order to coarsen the precipitates, these sheets were successively annealed at 1100 °C (β phase region) for 0.5 h, at 830 °C (α + β phase region) for 5 h, at 780 °C (α phase region) for 216 h, and then slowly cooled in the furnace in vacuum state.

### 2.2. Observation of precipitate

The micro-structures of the matrix were examined using a polarized optical microscope (Leica DMRX) and a SEM (JEOL JSM-6300) after the coarsening treatment. The precipitates in the matrix were also observed in detail with a TEM (JEOL JEM-2000FXII) equipped with energy dispersive X-ray spectroscopy (EDS).

Table 1
Chemical composition of the Zircaloy-4 in this study (wt%)

| Sn | Fe | Cr | O | Zr |
|---|---|---|---|---|
| 1.32 | 0.21 | 0.11 | 0.122 | Balance |

Metallic specimens for the optical microscope and the SEM were prepared using mechanical grinding to produce a mirror surface using 1200 Grid SiC paper and chemical etching with a solution of 10% HF, 45% $HNO_3$, and 45% $H_2O$. The specimens for the TEM were prepared at −45 °C (applied voltage and current = 12 V/1.2 mA) by the twin-jet polisher (Struers, Tenupol-3) using a solution of 10% $HClO_3$ and 90% $C_2H_5OH$ after mechanical thinning to 70 μm.

### 2.3. Corrosion tests

The heat-treated materials were machined to a size of $20 \times 25 \times 2$ mm$^3$ for the corrosion tests. The specimens were mechanically ground with 800 Grid SiC paper and chemically polished using a pickling solution (a mixture of 5% HF, 45% $HNO_3$, and 50% $H_2O$) in the final step. Corrosion tests were conducted in steam at a pressure of 10.3 MPa and temperature of 400 °C for 24 days in a static autoclave, in accordance with ASTM Practice for Aqueous Corrosion Testing of Samples of Zirconium and Zirconium Alloys Procedure (G2-88). To obtain samples with the specific oxide thickness of 1 μm (pre-transition regime) and 4 μm (post-transition regime), the weight gains were measured after every corrosion period. The thickness of the oxide film was calculated from the measured weight gain and confirmed by the SEM examination.

### 2.4. Observation of precipitate oxidation at the metal–oxide interface

To observe the oxide morphologies of oxide formed at the interface of the matrix and oxide, the metal part of the oxidized sample was removed chemically with the mentioned etchant. Then the precipitates in the vicinity of the interface were examined using an optical microscope and SEM. In addition, the depletion of Fe and Cr from precipitates in the vicinity of the interface was observed by the technique of line profile using an EPMA (Cameca SX-50) with a beam diameter of 0.1 μm, which was attached with wavelength dispersive X-ray spectroscopy (WDS) and EDS, for the oxidized sample of post-transition regimes.

### 2.5. Observation of oxide crystal structure

The crystal structure of the oxide layers was characterized by a grazing angle XRD using a synchrotron XRD of 3C2 beamline in Pohang Accelerator Lab., with the energy range of 4–12 keV and a beam size of less than 1 mm$^2$. The grazing angle of the incident beam was varied from 0.01° to 10° to identify the depth of tetragonal $ZrO_2$. The measurements were made at 0.02° intervals of $2\theta$ over a range of 25°–45° with a count-time

of 5 s at each angle. Integrated intensities were calculated for the measured X-ray peaks, and the intensity of the tetragonal $ZrO_2(1\,1\,1)$ peak was compared with that of the monoclinic $ZrO_2(\bar{1}\,1\,1)$ peak. The ratio of integrated intensities was not equal to the amount of tetragonal $ZrO_2$ or monoclinic $ZrO_2$ directly, but the ratio showed a relative change in the crystal structure.

### 2.6. Observation of precipitate oxidation on surface oxide

The distributions of Fe and Cr on the oxide surfaces were analyzed by using the line scanning method of SIMS (Cameca IMS-4F). Secondary positive oxygen ions were used for the line scanning with a beam diameter of 10 μm and a primary ion current of 10 nA. The concentration of Fe and Cr could not be compared with each other but the distribution of Fe and Cr could be analyzed from the variation of intensities for a single element.

## 3. Results

### 3.1. Micro-structures after the heat-treatments

Fig. 1 shows the micro-structures of the Zircaloy-4 matrix after heat-treatment to coarsen the precipitates. The precipitates existed mainly at the boundaries of prior β-phase grains. And the mean diameter of the precipitates increased up to 3 μm from about 0.1 μm, which was that of the as-received Zircaloy-4. But the number density of the precipitates decreased drastically. Since the solubility of Fe and Cr was very low in α-Zr, i.e. in the region of 120 ppm for Fe and 200 ppm for Cr at the maximum solubility temperature [16], most of the Fe and Cr in the α matrix should form the intermetallic precipitates of the $Zr(Fe,Cr)_2$. From the TEM micro-analysis in Fig. 2, it could be found that the precipitates revealed the structure of a hexagonal Laves phase (C14) and showed the characteristics of stacking faults as seen in the dark field image. The ratio of Fe to Cr was varied in the range of 1.2–1.7. The mean size of precipitates analyzed from the TEM image was about 2.7 μm in equivalent diameter.

### 3.2. Oxidation kinetics

As shown in Fig. 3, the weight gain kinetics of the heat-treated samples in 400 °C steam was similar to that of typical Zircaloy-4, expressing two regimes of pre-transition and post-transition. The change of pre-transition to post-transition occurred at the oxidation time of 6 days. It was believed that the parabolic kinetics in the pre-transition regime result from the non-homogeneity of the diffusion process controlling oxide growth.

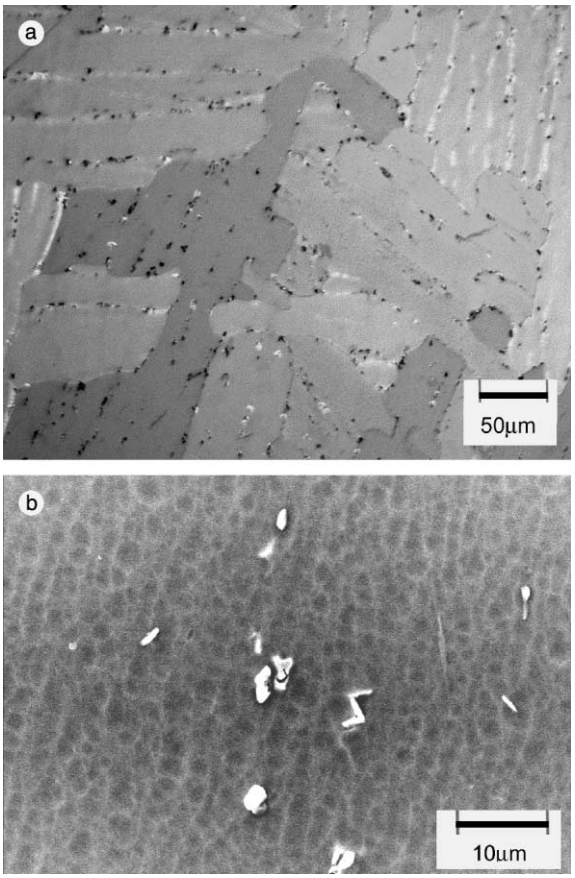


Fig. 1. Micro-structures of the Zircaloy-4 matrix after heat-treatment for coarsening the precipitates: (a) polarized optical microscope and (b) SEM.

When the oxide reached a thickness of about 2 μm, which was calculated from the measured weight gain (15 mg/dm$^2$∼1 μm), the oxidation rate was approximately constant.

It was reported that the change in kinetics to the post transition linear rate is smooth and no sudden discontinuities are observed at relative high temperatures ($\geqslant$ 400 °C) [17]. Fortunately, it was obviously observed in this study that the transition of the oxidation rate occurred when the oxide thickness reached about 2 μm after the 6-day oxidation test. For the verification of the depletion rate of Fe and Cr within the precipitates, two oxidized samples having an oxide thickness of ∼1 μm (the pre-transition) and ∼4 μm (post-transition regimes) were selected.

### 3.3. Morphologies of interfacial oxide

After the oxidation test in 400 °C steam, the initiated oxide samples were prepared by etching out the metal part for the observation of the precipitates in the oxide

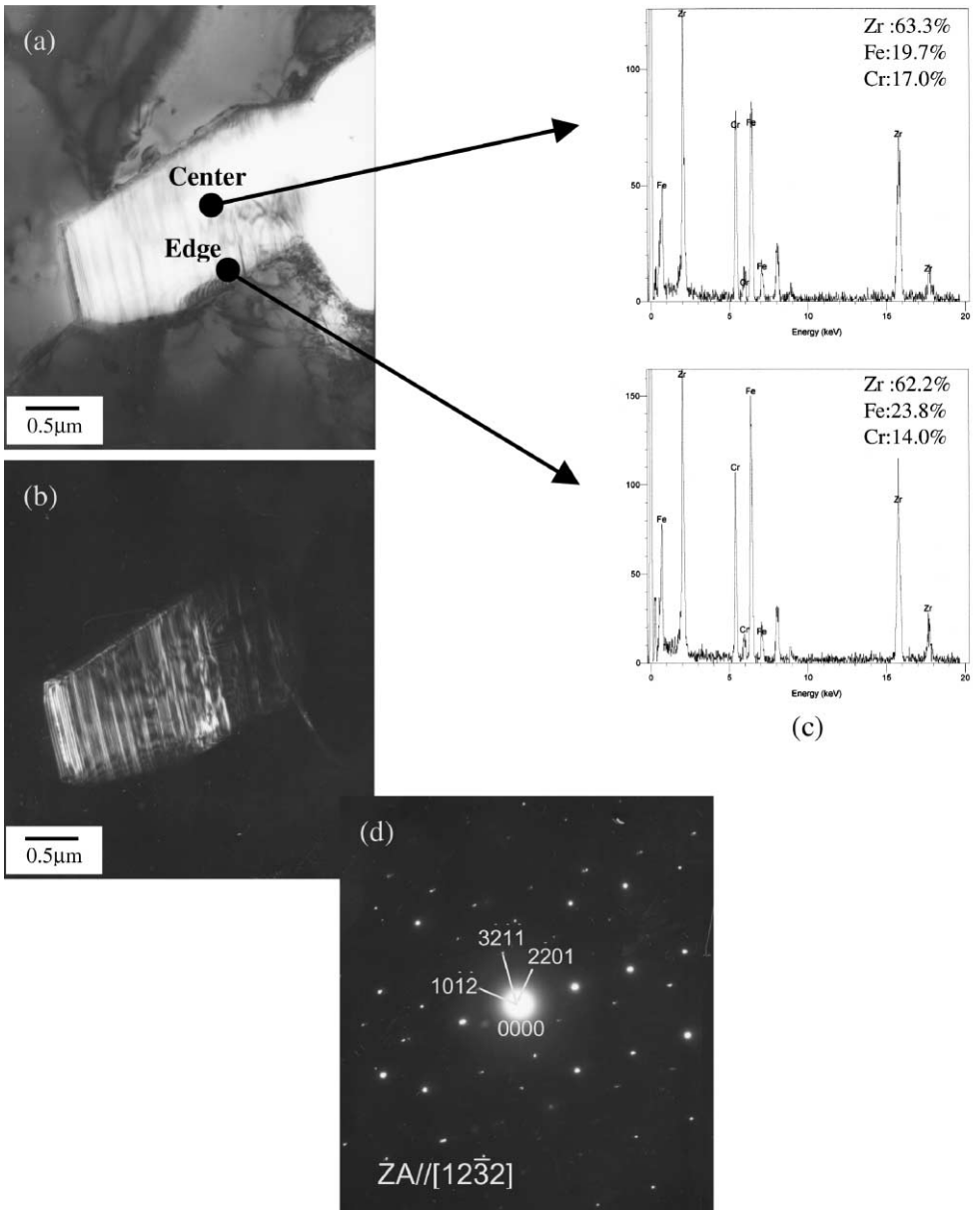


Fig. 2. TEM micro-analysis of a coarsening precipitate in the heat-treated Zircaloy-4 matrix: (a) bright field image, (b) dark field image, (c) EDX spectra at center and edge and (d) SAD pattern of the precipitate.

interfacing with the matrix. In Fig. 4 of the post-transition oxide sample, the morphology in the initiated oxide part showed a diffuse-out image. The precipitates in the oxide could not be distinguished clearly from the zirconium oxide. The diffuse-out image resulted from the precipitate oxidation. It was interpreted that the oxidation rate of precipitates is slower than that of the Zr matrix.

A SEM was used to examine in detail the initiated oxide and the results were disclosed in Fig. 5. Unoxidized precipitates were observed in Zr oxide in both the pre- and post-transition regimes. The unoxidized precipitates existed only in the vicinity of the matrix–oxide interface in the case of the post-transition sample while the precipitates were observed in the regions far away from the interface in the case of the pre-transition. The size of the precipitates was reduced with increasing oxidation time. This decrease of the precipitate size would be resulted from the oxidation of the precipitates in the oxide layer.

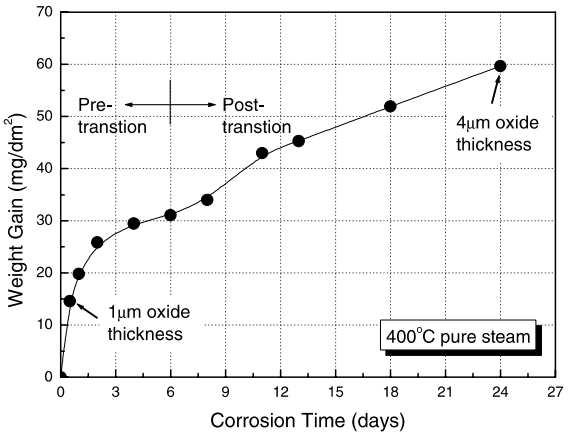


Fig. 3. Corrosion behavior in the condition of 400 °C steam of the heat-treated Zircaloy-4 for coarsening the precipitates.

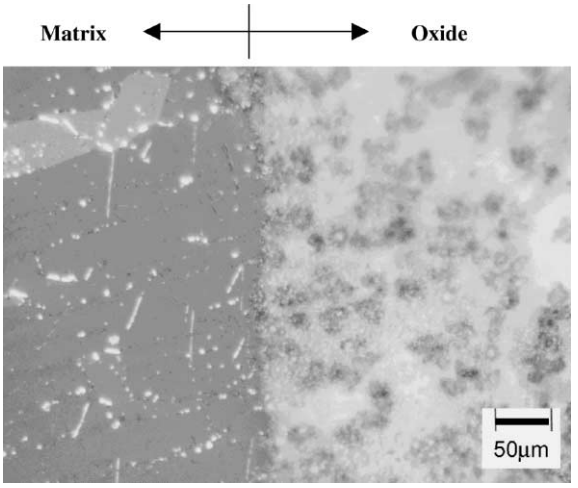


Fig. 4. Micro-structure of the initiated oxide at the matrix and oxide interface of the post-transition sample (4 μm in oxide thickness).

### 3.4. Electron probe micro-analyzer analysis

For the oxidized sample with 4 μm in oxide thickness (post-transition), the EPMA line profiles at the interface between the matrix and oxide are revealed in Fig. 6. Two precipitates at the interface were selected to verify the oxidation kinetics of Fe and Cr in the precipitates. The one (P1 in Fig. 6) was located in matrix and the other (P2 in Fig. 6) in the oxide. There was no difference in the size (about 2 μm) of the two precipitates. Since the intensities of the two elements (Fe and Cr) were normalized on the basis of the intensity of Zr, the concentration of the elements in the precipitates could be interpreted indirectly from the measured intensities. The intensity of Fe in the two precipitates was different while that of Cr

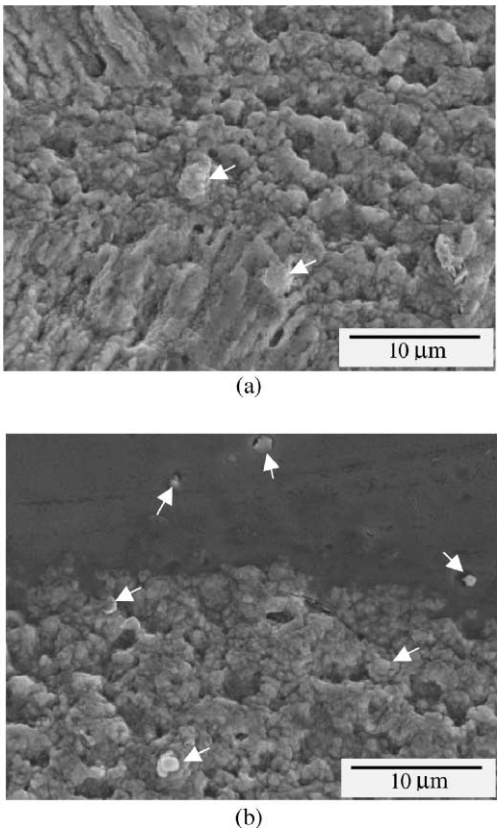


Fig. 5. SEM morphologies at interfacial oxide of the oxidized samples with (a) 1 μm and (b) 4 μm in oxide thicknesses.

remained almost constant regardless of the locations. The Fe intensity in the P1 of the matrix precipitate was stronger than that in the P2 of the oxide precipitate. This means that the oxidation kinetics of Fe and Cr could be different within precipitates. The difference of the Fe intensities between the two precipitates could result from the faster rate of Fe oxidation. It was confirmed that the oxidation rate of Fe within precipitates is faster than that of Cr.

### 3.5. Synchrotron X-ray diffractometer analysis

It is understood that tetragonal $ZrO_2$, a meta-stable phase formed from the high Pilling-Bedworth ratio of Zr (1.56) at the interface of matrix and oxide affects the oxidation kinetics of Zr in the oxidation process [18–21]. The tetragonal $ZrO_2$ phase acts as a barrier layer to control the oxidation rate. The crystal structure transformation from the tetragonal $ZrO_2$ to the monoclinic $ZrO_2$ results in the acceleration of the oxidation rate. To verify the location of the tetragonal $ZrO_2$ in the oxide layer, the synchrotron XRD analysis was performed by varying the grazing angle for the oxidized samples in the

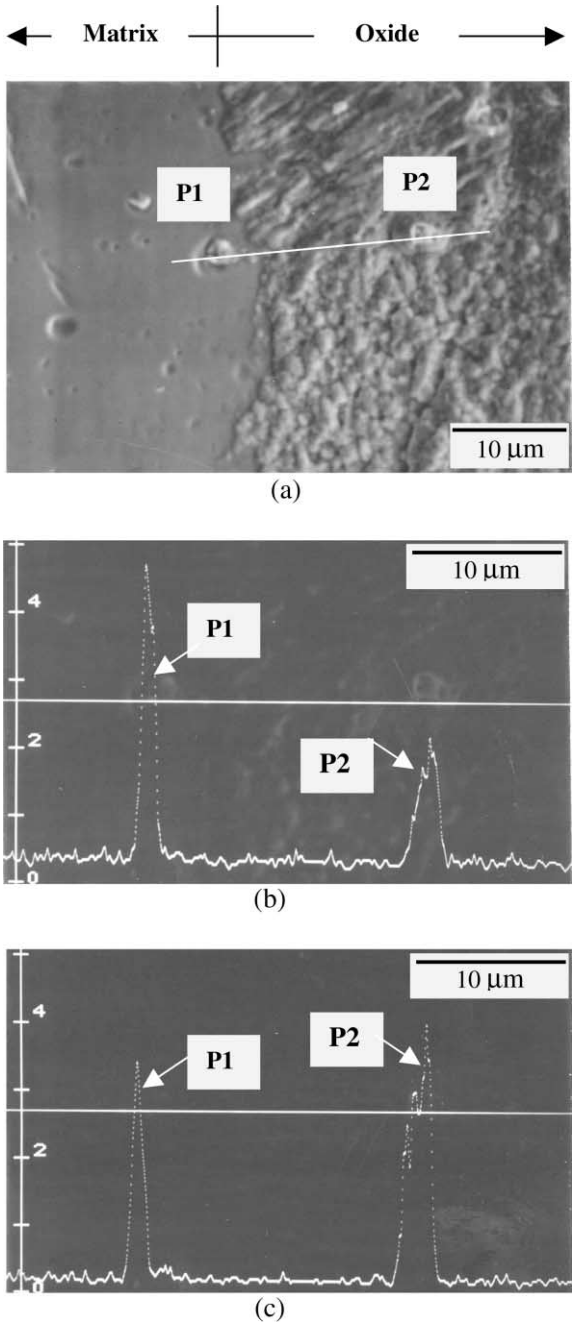


Fig. 6. Line profiles of Fe and Cr in precipitates at interfacial oxide of the oxidized sample with 4 μm in oxide thickness: (a) SEM image, (b) Fe profile and (c) Cr profile.

regime of the pre- (1 μm oxide thickness) and post-transition (4 μm oxide thickness) and the resulting patterns are shown in Fig. 7.

The penetration depth of the X-ray in the oxide layer can be changed with the variation of the grazing angle of the incident beam. Especially, the grazing angle was linearly related to the penetration depth in the case of a small grazing angle of less than 10°. In the case of the oxidized sample of the pre-transition regime, the intensity of tetragonal (1 1 1)-$ZrO_2$ was changed by increasing the grazing angle of the incident beam and the intensity maximum of the tetragonal oxide occurred at the grazing angle of 1°. The tetragonal $ZrO_2$ intensity at the grazing angle 2° was reduced slightly from the maximum by increasing the maximum peak intensity. This trend also appeared in the post-transition sample. But the intensity maximum occurred at the grazing angle of 5° in the post-transition oxide. The ratio of tetragonal (1 1 1)-$ZrO_2$ to monoclinic $(\bar{1}\,1\,1)$-$ZrO_2$ was calculated by integrating the peaks and is summarized in Table 2. It is thought that the intensity maximum will occur when the penetration depth of the X-ray is equivalent to the thickness of the oxide layer because the tetragonal $ZrO_2$ exists in the thin oxide layer of the interface between the matrix and oxide.

### 3.6. Secondary ion mass spectroscope analysis

Both the oxidized samples with 1 and 4 μm of oxide thickness were analyzed on the oxide surface by the SIMS line profiling technique. The profiles on the oxide surface are shown in Fig. 8. The level of Fe and Cr on the surface was not quantified but the line profiles could only represent the relative localization of the alloying elements. It was considered that the concentrated sites of Fe and Cr would agree with the sites of the precipitates because of the low solubility of Fe and Cr in the Zr matrix. Most Fe and Cr would be located in precipitates. In the case of the pre-transition oxide with a 1 μm thickness, the profiles of Fe and Cr on the oxide surface nearly coincide with each other. The peaks in the Cr profile were shown at the same positions of the peaks in the Fe profile. Fe and Cr were concentrated in the positions of the precipitates. In the case of the post-transition oxide with a 4 μm thickness, the peaks in the Fe profile disappeared but the peaks in the Cr profile could be observed on the oxide surface. This was interpreted to mean that the Fe on the surface oxide was already oxidized in the regime of post-transition. The oxidation of Fe within precipitates would be faster than Cr in the view of the oxidation rate.

## 4. Discussion

It has been reported in many studies that the precipitates can control the uniform oxidation rate of the Zircaloy-4 alloy [1–14]. Since the oxidation rate of precipitates was slower than that of the Zr matrix, the larger precipitates could retard the uniform oxidation of

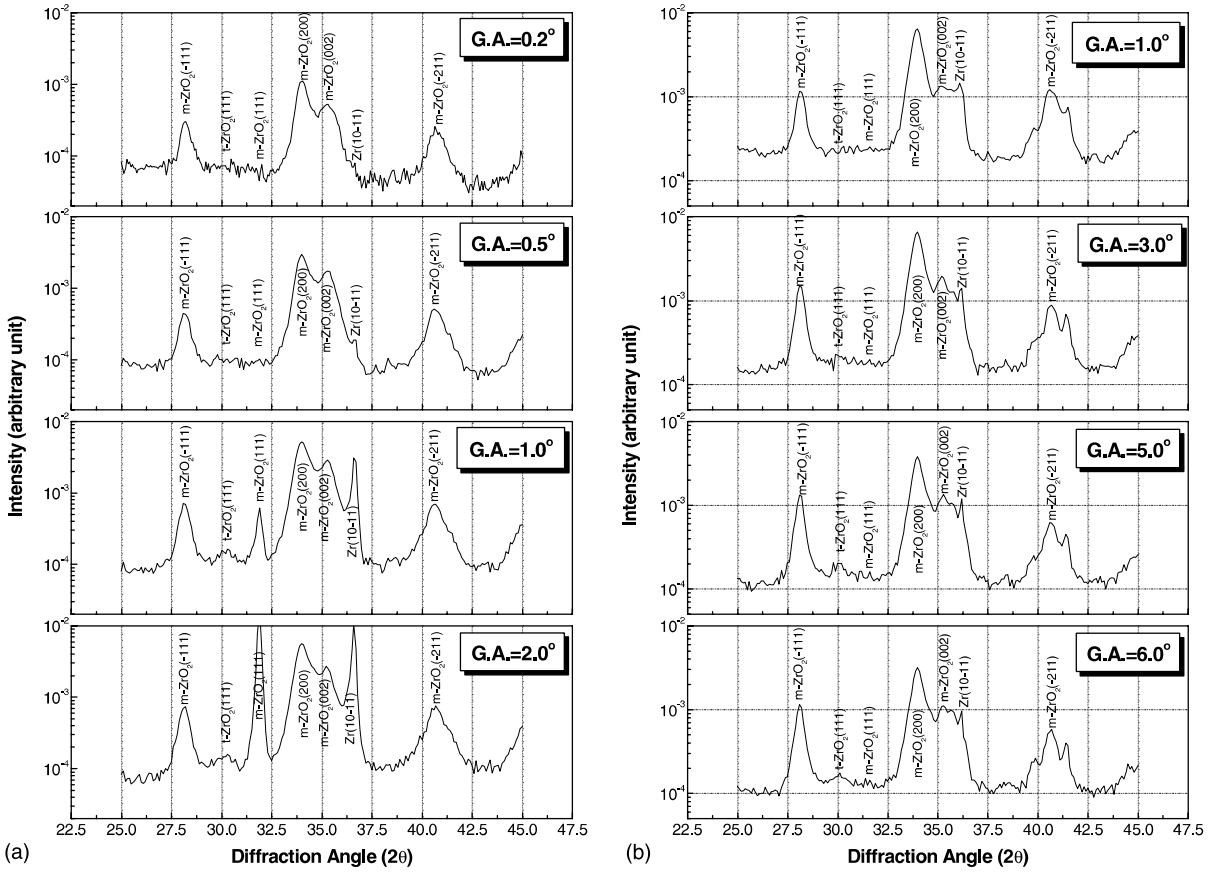


Fig. 7. Synchrotron XRD patterns of the oxides on the oxidized samples with (a) 1 μm and (b) 4 μm in oxide thicknesses.

Table 2
Ratio of (1 1 1) $t$-$ZrO_2$ to ($\bar{1}$ 1 1) $m$-$ZrO_2$ in the oxide layer

| Pre-transition (~1 μm in oxide thickness) | | Post-transition (~4 μm in oxide thickness) | |
|---|---|---|---|
| Grazing angle | Ratio | Grazing angle | Ratio |
| 0.2° | 0 | 1° | 0 |
| 0.5° | 0.02 | 3° | 0.03 |
| 1° | 0.06 | 5° | 0.06 |
| 2° | 0.02 | 6° | 0.04 |

Zircaloy-4. The larger precipitates could improve the uniform corrosion resistance of the alloy. And some researchers explained the oxidation of incorporated precipitates into oxide could give rise to a transformation of the structures from monoclinic $ZrO_2$ to tetragonal $ZrO_2$ or cubic $ZrO_2$ of the surrounding oxide [7–9,11].

As explained in the proceeding section, the oxidation kinetics of alloying elements such as Fe and Cr within precipitates has been characterized for Zircaloy-4. The oxidation rates of the alloying elements could control the total oxidation rate of the alloy. The structure of the precipitates, in Fig. 2, was identified as hcp $Zr(Fe, Cr)_2$ by SAD analysis of TEM and the ratio of Fe to Cr was in the range of 1.2–1.7. After the heat-treatment was performed to coarsen the precipitates of Zircaloy-4, the oxidation kinetics of the heat-treated samples almost agreed with that of the as-received (typical) Zircaloy-4 [22]. It could be said the heat-treatment did not affect the oxidation kinetics of the alloy. In other words, the oxidation kinetics were represented by two regimes of pre- and post-transition.

From the micro-structure observation at the interface between the matrix and oxide in Figs. 4 and 5, most precipitates in the regime of post-transition were gradually oxidized and the smaller precipitates existed in the interfacial oxide, compared to the precipitates in the pre-transition regime. This could be interpreted that the Zr matrix would be oxidized earlier than the precipitates, the unoxidized precipitates would be incorporated in the interfacial oxide, and then the incorporated precipitates in the oxide would be oxidized gradually. The overall corrosion rate of Zircaloy-4 could be governed mostly by the oxidation of precipitates.

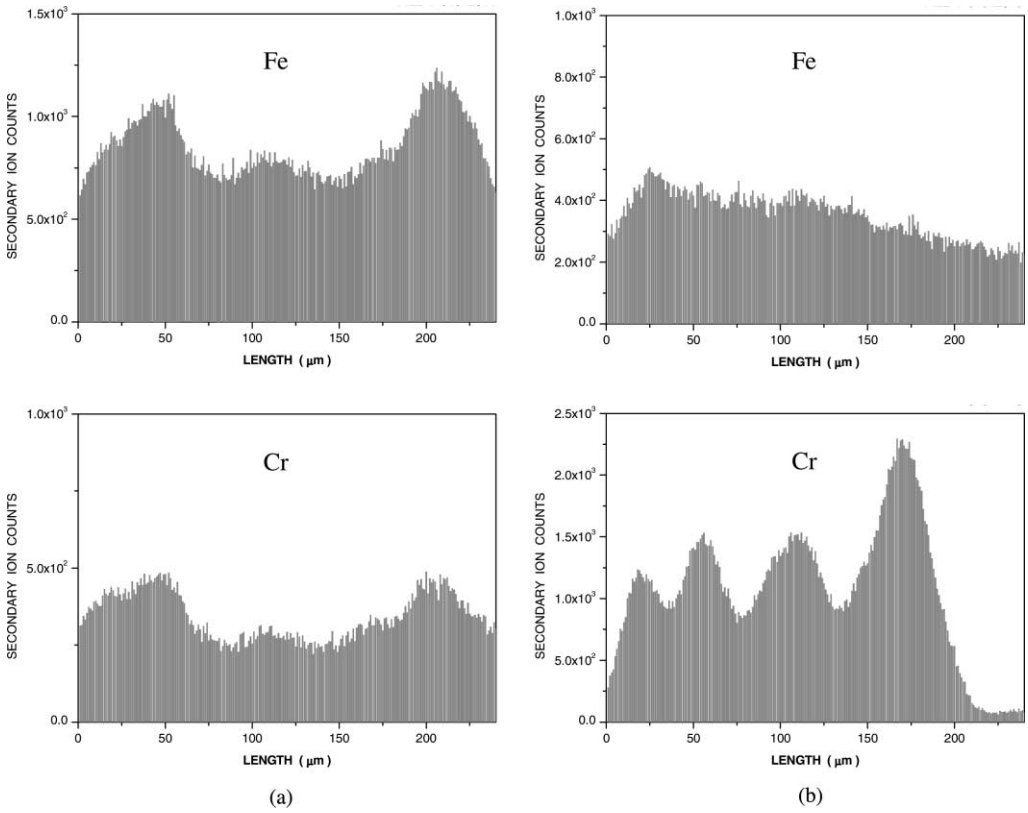


Fig. 8. SIMS line profiles on the surface oxides of the oxidized samples with (a) 1 μm and (b) 4 μm in oxide thicknesses.

The oxidation rates of Fe and Cr within precipitates were different as found by the techniques of EPMA and SIMS. From the two techniques, it was found that the oxidation rate of Fe was faster than that of Cr within the precipitates of Zircaloy-4. The difference of the oxidation rate between Fe and Cr could be explained by the decrease of the Fe to Cr ratio within incorporated precipitates in oxide during the oxidation process. According to the Pecheur et al. some iron within precipitates would be dissolved into the $ZrO_2$ matrix [7,8]. Since both compressive stress and adequate alloying elements such as iron are known to stabilize tetragonal $ZrO_2$, the iron dissolution into the $ZrO_2$ matrix would contribute to extend the stabilization of tetragonal $ZrO_2$ in the interfacial oxide layer. So, the slower oxidation rate of Fe than Cr would be correlated to the corrosion kinetics of Zircaloy-4.

In addition, for the taped oxide layer by SIMS ionic image, Garzarrolli et al. observed the localization of Fe and Cr in the oxide of Zircaloy-4 [11]. They suggested that the Fe distribution is more soluble than that of Cr. These trends agreed with our analysis results by EPMA and SIMS. Accordingly, it was considered that the Fe within the incorporated precipitates in the oxide is oxidized earlier than the Cr. It could be thought that the Fe oxidation within the incorporated precipitates might play a key role in controlling the overall oxidation rate of Zircaloy-4.

In Zircaloy-4, the oxidation sequence can be explained by the above considerations. When oxidized in 400 °C steam, the Zr matrix is oxidized earlier rather than the precipitates. The unoxidized precipitates could be incorporated in the oxide. Then the Fe within the incorporated precipitates would be oxidized before the oxidization of Cr. Finally, Cr would be oxidized in the oxide. This Fe dissolution into $ZrO_2$ matrix would contribute the formation of tetragonal $ZrO_2$ in surrounding oxides. So, the oxidation of samples having larger precipitates would be retarded in Zircaloy-4 because the larger precipitates could form the larger area to be stabilized tetragonal $ZrO_2$ in the surrounding oxides. This hypothesis could be applied to the results of the present study.

Godlewski proposed that the fraction of tetragonal $ZrO_2$ in oxide was related to the corrosion rate and transition of the corrosion rate of Zircaloy-4 [18]. He pointed out that the fraction increased slightly due to the generation of a compressive stress field and changed drastically at a transition point during the precipitate oxidation. As mentioned by Pecheur et al. the segrega-

tion of Fe and Cr in precipitates could stabilize the tetragonal $ZrO_2$ phase because of the delayed oxidation of alloying elements such as Fe and Cr with respect to the Zr in precipitates [7,8]. The synchrotron XRD analysis in Fig. 7 supported the assumption that the tetragonal $ZrO_2$ layer exists at the most inner oxide layer in the vicinity of the matrix–oxide interface by the observation of the tetragonal $ZrO_2$ at a specific grazing angle. This tetragonal $ZrO_2$ phase layer would act as a barrier layer, obstructing the diffusion of the oxygen ion. The precipitates were not fully oxidized in the $ZrO_2$ layer as evidenced by the traces of precipitates on the oxide surface observed by SIMS.

It is possible to suggest the oxidation kinetics of precipitates from the experimental results. Fig. 9 shows the schematic diagram of precipitate oxidation in the vicinity of the matrix–oxide interface of Zircaloy-4. The $Zr(Fe, Cr)_2$ type precipitate was incorporated in the oxide because the precipitates were oxidized slower than the Zr matrix. It is thought that the structure of the initial oxide is tetragonal $ZrO_2$ phase, providing a barrier layer for the diffusion of the oxygen ion. In the initial oxide, a small amount of Fe would be dissolve into the surrounding oxide. In the process of the Fe dissolution into the oxide matrix, the tetragonal $ZrO_2$ would be more stabilized by the oxidation of Fe at the boundary of the precipitates. With the oxidation time increased, most of the Fe as well as a little of the Cr would dissolve into the oxide and a few of Cr would start to dissolve into the oxide. Simultaneously, the oxide structure would be transformed from the tetragonal $ZrO_2$ phase to the monoclinic $ZrO_2$ phase due to the oxidation of Fe and Cr. The Fe-depleted precipitate in this step should be left in the oxide layer. The Fe within precipitates would be oxidized to iron oxide simultaneously. The volume expansion caused by the oxidation of Fe in the oxide could have contributed to the formation of compressive stress in the oxide layer. Beyond a critical compressive stress to stabilize the tetragonal oxide phase, the excess stress would result in the motive for the phase transformation from tetragonal $ZrO_2$ to monoclinic $ZrO_2$. The TEM observation on the oxide layer was not conducted for the phase transformation in this study, but the existence of micro-cracks in the middle oxide was already discussed in previous studies [23,24]. The micro-cracks would also be developed in the oxide layers, which could be evidence of stress relaxation in oxide.

At the further outer oxide layer, most of the Fe would have oxidized into the surrounding oxide and then Cr from the precipitates would have oxidized into the oxide matrix. After the Fe within the precipitates was utterly exhausted in the oxide matrix, the Cr within the precipitates would also be oxidized gradually into the surrounding oxide.

It was concluded that the oxidation rate of Fe was much faster than that of Cr within precipitates. The Fe dissolution in the initial stage could stabilize the tetragonal $ZrO_2$ phase of the surrounding oxide and the oxidation of Fe and Cr would be thought to give rise to a transformation from tetragonal $ZrO_2$ to monoclinic $ZrO_2$. All Fe in precipitates would be preferably oxidized out and then Cr would be oxidized gradually.

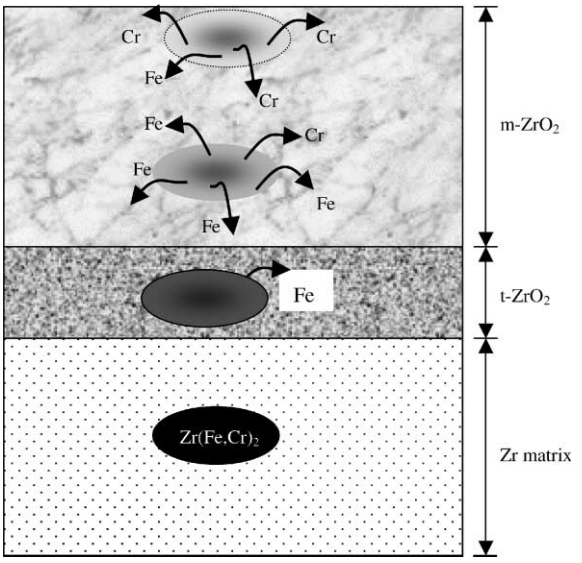


Fig. 9. Schematic diagram of precipitate corrosion in the vicinity of the matrix–oxide interface of Zircaloy-4.

## 5. Conclusions

The oxidation kinetics of precipitates in the oxide layer formed in 400 °C steam have been studied by the techniques of OM, SEM, EPMA, Synchrotron XRD, and SIMS. The Zr matrix was oxidized earlier than the precipitates, so the unoxidized precipitates would incorporate in oxide, and then the incorporated precipitates in oxide would be oxidized gradually. The overall corrosion rate of Zircaloy-4 could be governed mostly by the oxidation of precipitates. In precipitates, the alloying elements such as Fe and Cr exhibited a difference in their oxidation rate, that of Fe being much faster than that of Cr within the precipitates. It was interpretated that the Fe dissolution in the initial stage could have stabilized the tetragonal $ZrO_2$ phase of the surrounding oxide, and then the oxidation of Fe and Cr would have initiated the phase transformation from tetragonal $ZrO_2$ to monoclinic $ZrO_2$ when the excess compressive stress was created due to the oxidation of Fe and Cr within precipitates.

It was concluded that the oxidation kinetics were dependent on the depletion of alloying elements such as

Fe and Cr from precipitates. In the first stage, the Fe dissolution into $ZrO_2$ matrix and its oxidation would lead to enhance the stabilization of the tetragonal $ZrO_2$ phase in the interfacial oxide. As the oxidation processed, the tetragonal $ZrO_2$ phases would transform to the monoclinic $ZrO_2$ phases beyond the critical compressive stress. At the later stage, the oxidation of Fe and Cr in precipitates was responsible for the destabilization of the tetragonal $ZrO_2$ phase.

## Acknowledgements

This project has been carried out under the Nuclear R&D Program by MOST.

## References

[1] G. Garzarrolli, H. Stehle, E. Steinberg, H.G. Weidinger, in: R.B. Adamson, L.F.P. Van Swam (Eds.), Zirconium in the Nuclear Industry: Seventh International Symposium, ASTM STP 939, American Society for Testing and Materials, 1987, p. 417.
[2] G. Garzarrolli, E. Steinberg, H.G. Weidinger, in: L.F.P. Van Swam, C.M. Eucken (Eds.), Zirconium in the Nuclear Industry: Eighth International Symposium, ASTM STP 1023, American Society for Testing and Materials, 1989, p. 202.
[3] P. Rudling, H. Pettersson, T. Andersson, T. Thorvaldsson, in: L.F.P. Van Swam, C.M. Eucken (Eds.), Zirconium in the Nuclear Industry: Eighth International Symposium, ASTM STP 1023, American Society for Testing and Materials, 1989, p. 213.
[4] T. Andersson, T. Thorvaldsson, A. Wilson, A.M. Wardle, IAEA-SM-288/59, 1989, p. 435.
[5] J.P. Gros, J.F. Wadier, J. Nucl. Mater. 172 (1990) 85.
[6] Y.H. Jeong, Korean J. Mater. Res. 6 (6) (1996) 584.
[7] D. Pecheur, F. Lefebvre, A.T. Motta, C. Lemagnan, D. Charquet, in: A.M. Garde, E.D. Bradley (Eds.), Zirconium in the Nuclear Industry: Tenth International Symposium, ASTM STP 1245, American Society for Testing and Materials, 1994, p. 687.
[8] D. Pecheur, F. Lefebvre, A.T. Motta, C. Lemagnan, J.F. Wadier, J. Nucl. Mater. 189 (1992) 318.
[9] X. Iltis, F. Lefebvre, C. Lemagnan, J. Nucl. Mater. 224 (1995) 121.
[10] M. Harada, M. Kimpara, K. Abe, in: C.M. Eucken, A.M. Garde (Eds.), Zirconium in the Nuclear Industry: Ninth International Symposium, ASTM STP 1132, American Society for Testing and Materials, 1991, p. 368.
[11] F. Garzarolli, H. Seidel, R. Tricot, J.P. Gross, in: C.M. Eucken, A.M. Garde (Eds.), Zirconium in the Nuclear Industry: Ninth International Symposium, ASTM STP 1132, American Society for Testing and Materials, 1991, p. 395.
[12] H. Anada, K. Nomoto, Y. Shida, in: A.M. Garde, E.D. Bradley (Eds.), Zirconium in the Nuclear Industry: Tenth International Symposium, ASTM STP 1245, American Society for Testing and Materials, 1994, p. 307.
[13] H. Anada, B.J. Herb, K. Nomoto, S. Hagi, R.A. Graham, T. Kuroda, in: E.D. Bradley, G.P. Sabol (Eds.), Zirconium in the Nuclear Industry: Eleventh International Symposium, ASTM STP 1295, American Society for Testing and Materials, 1996, p. 74.
[14] J.H. Baek, Y.H. Jeong, I.S. Kim, J. Nucl. Mater. 280 (2000) 235.
[15] B. Wadman, Z. Lai, H.-O. Andren, A.-L. Nylstorm, P. Rudling, H. Pettersson, in: A.M. Garde, E.D. Bradley (Eds.), Zirconium in the Nuclear Industry: Tenth International Symposium, ASTM STP 1245, American Society for Testing and Materials, 1994, p. 579.
[16] D. Chaarquest, R. Hahn, E. Ortlieb, E. Gros, J.P. Wadier, in: L.F.P. Van Swam, C.M. Eucken (Eds.), Zirconium in the Nuclear Industry: Eighth International Symposium, ASTM STP 1023, American Society for Testing and Materials, 1989, p. 405.
[17] J.K. Dawson, G. Long, W.E. Seddon, J.F. White, J. Nucl. Mater. 25 (1968) 179.
[18] J. Godlewski, in: A.M. Garde, E.D. Bradley (Eds.), Zirconium in the Nuclear Industry: Tenth International Symposium, ASTM STP 1245, American Society for Testing and Materials, 1994, p. 663.
[19] H.-J. Beie, A. Mitwalsky, F. Garzarolli, H. Ruhmann, H.-J. Sell, in: A.M. Garde, E.D. Bradley (Eds.), Zirconium in the Nuclear Industry: Tenth International Symposium, ASTM STP 1245, American Society for Testing and Materials, 1994, p. 615.
[20] H. Anada, K. Takeda, in: E.D. Bradley, G.P. Sabol (Eds.), Zirconium in the Nuclear Industry: Eleventh International Symposium, ASTM STP 1295, American Society for Testing and Materials, 1996, p. 35.
[21] B. Cox, AECL Rep. 9382, Atomic Energy of Canada, Chalk River Nuclear Laboratories, 1987.
[22] J.H. Schemel, D. Charquet, J.-F. Wadier, in: L.F.P. Van Swam, C.M. Eucken (Eds.), Zirconium in the Nuclear Industry: Eighth International Symposium, ASTM STP 1023, American Society for Testing and Materials, 1989, p. 141.
[23] Y.H. Jeong, J.H. Baek, S.J. Kim, H.G. Kim, H. Ruhmann, J. Nucl. Mater. 270 (1999) 322.
[24] Y.H. Jeong, J.H. Baek, S.J. Kim, K.H. Kim, B.K. Choi, J.K. Bang, J. Korean Inst. Metal. Mater. 36 (7) (1998) 1138.